Shirasu *et al. Journal of Electric Propulsion* (2023) 2:11
https://doi.org/10.1007/s44205-023-00047-w

Journal of Electric Propulsion

RESEARCH Open Access

Demonstration and experimental characteristics of a water-vapor Hall thruster

Kento Shirasu[1*], Hiroki Kuwabara[1], Masayuki Matsuura[2], Hiroyuki Koizumi[2], Yuichi Nakagawa[3], Hiroki Watanabe[3], Hokuto Sekine[1] and Kimiya Komurasaki[1]

*Correspondence: shirasu-kento994@g.ecc.u-tokyo.ac.jp

[1] Department of Aeronautics and Astronautics, The University of Tokyo, Bunkyo-ku 113-8656, Tokyo, Japan
[2] Department of Advanced Energy, The University of Tokyo, Kashiwa-shi 277-8561, Chiba, Japan
[3] Pale Blue, Inc., Kashiwa-shi 277-0882, Chiba, Japan

Abstract

Water is an attractive candidate for condensable propellants owing to its availability, handleability, and sustainability. This study proposes the use of water vapor as a propellant for a low-power Hall thruster, and experimentally demonstrates the feasibility of this proposal. Based on the performance estimation from the plume diagnostics, a thrust-to-power ratio of 19 mN/kW, specific impulse of 550–860 s, and anode efficiency of 5–8 % were obtained at an anode power of 233–358 W. From further efficiency analysis, the mass utilization efficiency of water was found to be the most deteriorated among the internal efficiencies compared to the conventional xenon propellant, which was consistent with the expectations from a small discharge current oscillation, large beam divergence, and increase in low-energy ions. Moreover, additional power loss via reactions unique to polyatomic molecules was indicated by evaluation of the ionization cost. In this experiment, the mass utilization efficiency was improved with an increase in the anode voltage from 200 to 240 V without degradation of the power utilization. This suggests that operating at a higher voltage is more suitable for a water-vapor Hall thruster.

Keywords: Hall thruster, Water propulsion, Water-vapor plasma, Small spacecraft

Introduction

Small spacecraft have been widely used for different purposes, including deep-space exploration and large-scale constellations [1, 2]. To perform these innovative activities, small propulsion systems must be installed to provide high total impulse for station keeping, attitude control, and orbit transfer. The miniaturization of electrostatic propulsion thrusters such as gridded ion thrusters and Hall thrusters is the most promising approach because of their abundant flight heritage. The Hayabusa and Hayabusa2 missions successfully demonstrated sample returns from asteroids in deep space using several-hundred Watt ion thrusters [3, 4]. In 2020, Space Exploration Technologies Corp. started a networking service using small satellites flying in low orbit with Hall thrusters. Currently, even lower power, approximately 100 W or less, has been explored with the increase of micro-sized spacecraft [5–9].

Examples have already been demonstrated in the orbit [10, 11]; however, they are not yet generally used for practical applications. One of the causes is a number of additional

Springer

© The Author(s) 2023. **Open Access** This article is licensed under a Creative Commons Attribution 4.0 International License, which permits use, sharing, adaptation, distribution and reproduction in any medium or format, as long as you give appropriate credit to the original author(s) and the source, provide a link to the Creative Commons licence, and indicate if changes were made. The images or other third party material in this article are included in the article's Creative Commons licence, unless indicated otherwise in a credit line to the material. If material is not included in the article's Creative Commons licence and your intended use is not permitted by statutory regulation or exceeds the permitted use, you will need to obtain permission directly from the copyright holder. To view a copy of this licence, visit http://creativecommons.org/licenses/by/4.0/.

constraints on the propellant selection. Conventionally, xenon is the most popular propellant because of its large ionization cross-section, chemical inertness, large molecular mass, and high density in the supercritical fluid state. Each of these features contributes to achieving a high thrust efficiency, using an efficient hollow cathode, offering a moderate thrust force, and reducing the volume of the propellant tank, respectively. However, xenon has a major disadvantage in its high price. Because only minimal xenon is contained in the atmosphere, its production is relatively limited. Nevertheless, the consumption of xenon is increasing with the growth of space engineering, the medical industry, and semiconductor technology, which further increases the costs of its procurement. A large amount of propellant is typically consumed not only in orbit, but also in pre-ground testing; hence, expensive propellants are not the preferred choice especially for small spacecraft to reduce its development cost. Necessity of a high-pressure system also restrict the installation of xenon in terms of safety and structural mass. In the majority of cases, small spacecraft are launched with other payloads using rideshare opportunities, and installing a high-pressure tank with a potential risk of explosion is not recommended. Even if the system is adapted to the requirements for safety compliance, a significant increase in extra mass becomes a critical issue for small applications [10, 12]. These negative aspects of xenon encourage us to search for other propellants more suitable for small spacecraft.

Alternative propellants should be densely stored without a high-pressure system. From this perspective, condensable propellants, which can be stored in solid or liquid states and used as vapors, have attracted attention. Some metal and nonmetal materials have already been investigated [13–16], and iodine is currently regarded as the most practical candidate because of its low boiling temperature, low toxicity, and ionization properties close to those of xenon. However, iodine systems have other issues owing to their corrosiveness. For example, cathode corrosion is directly related to shorter lifetime [17, 18]. In addition, all components of a spacecraft should be compatible with iodine, and specific test facilities should be used for the safe exhaust of iodine vapor [17, 19, 20], both of which increase the cost and time for development.

Water is another candidate for condensable propellants and has unique affinities for small spacecraft [21–25]. The primary benefit of water is its inexhaustible abundance on Earth. This ensures that it will be sustainably available with negligible costs in the future. Water is also not harmful to human health and the environment, and can be easily handled in regular test facilities. Furthermore, the vapor pressure of water is considerably greater (more than 1 kPa at room temperature) than that of other condensable candidates including iodine. This also implies that the vaporization and feeding system can be manipulated near room temperature, which is convenient for microdevices with a small heat capacity. Although such suitability has provoked the studies of gridded ion thrusters using water as the propellant [25–28], only a limited number of studies have investigated water as a propellant for electrostatic propulsions because of three essential drawbacks: a small ionization cross-section, a relatively small ion mass, and strong oxidation. An ionization cross-section is directly related to propellant utilization, and the smaller it is, the more propellant should be consumed to generate sufficient plasma. Even though such a waste of mass is predicted, the specific impulse could be equal to or greater than the common values ($\gtrsim$ 1000 s) due to the small ion mass, but this is a

trade-off for inevitably low thrust; hence, longer duration would be required to achieve a high total impulse. Conversely, the oxidation of a cathode emitter impairs the system lifetime [29]; this has been considered a conflicting issue. Recently, however, remarkable cathode techniques that are adaptable to water propulsion have been progressing. One possible solution is to apply an emitter-free electron source using radio-frequency or electron cyclotron resonance (ECR) discharge. Nakagawa et al. demonstrated an ECR cathode worked using water-vapor plasma as a neutralizer for a gridded ion thruster [25]. Another approach is to use pure hydrogen obtained through water electrolysis for hollow cathode operation, as proposed by Schwertheim et al. [30] As the development of water-compatible cathodes continues to advance, it has become more valuable to pioneer low-power electrostatic propulsion thrusters using water and assess their usability as miniature primary propulsions.

Among flight-proven electrostatic propulsions, Hall thrusters are well suited for installation in small spacecraft owing to their simplicity and robustness [31]. Plasma production and beam neutralization are performed using a single cathode, which reduces the number of power supplies and simplifies the electrical configuration. Because the produced ions are not accelerated through mechanical grids, but rather through a magnetic barrier, failures due to unexpected electrical conduction are unlikely to occur. This acceleration technique also provides a high beam density regardless of the space charge limit and contributes significantly to achieving a moderate thrust-to-power ratio, even with light-molecule propellants such as water. Prevalent Hall thrusters have an annular-shaped discharge channel; hence, simple geometrical downscaling leads to the deterioration of the performance and lifetime owing to a large surface-to-volume ratio [31, 32]. To suppress this negative effect, novel designs specialized for low power have been attempted [31], and currently, 100 W-class Hall thrusters have emerged that demonstrate a thrust efficiency similar to that of conventional sub-kW thrusters [33]. The technological growth of low-power Hall thrusters has motivated us to challenge the use of more innovative propellants.

In this study, we propose a Hall thruster that use water vapor as the propellant. As another approach, Schwertheim et al. previously proposed a water electrolysis Hall thruster, that fed the generated oxygen to the anode and hydrogen to the cathode [30]. However, mixing oxygen and hydrogen has a risk of explosive reactions and also requires strict propellant management. On the other hand, the direct use of water vapor preserves the inherent benefits of water and is more compatible with the high safety requirements of small spacecraft. To demonstrate the feasibility of our proposal, we experimentally operate a miniature Hall thruster using water vapor at a few-hundred Watt and measure the beam properties using two types of electrostatic probes. We also operate the same thruster with a conventional propellant, i.e., xenon, to highlight the unique features of the water propellant. The discharge and plume characteristics, and approximated performance are presented and discussed in this paper.

Experimental apparatus and analysis method

Miniature Hall thruster

A miniature thruster head was designed and developed in reference to an 85 W class xenon Hall thruster [9]. The structural schematic is displayed in Fig. 1 (a). The discharge

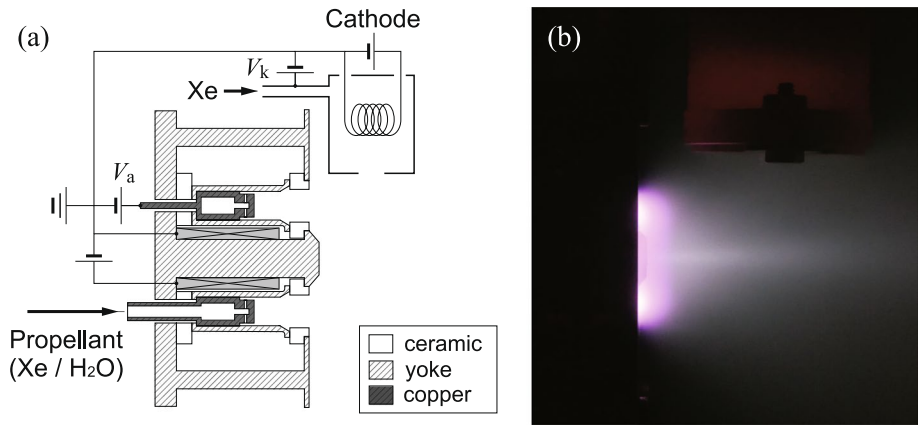

Fig. 1 (**a**) Structural and electrical schematic of the miniature Hall thruster and (**b**) plume appearance operated with water vapor

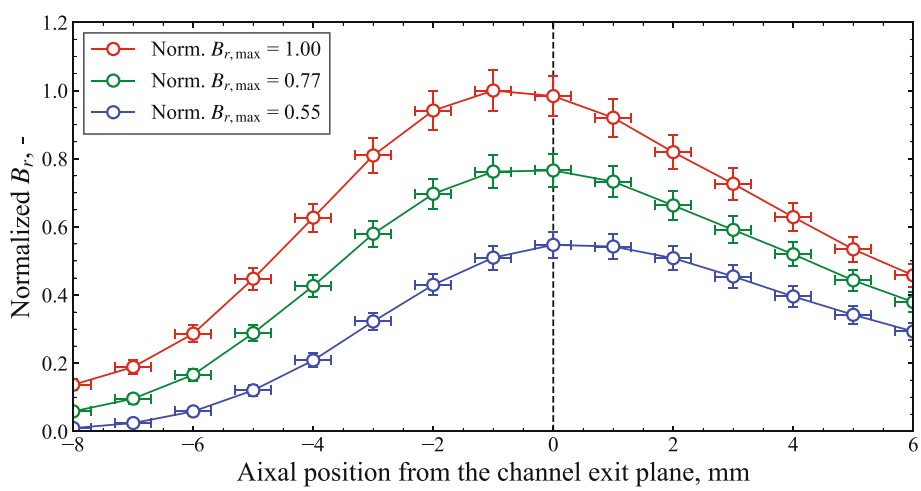

Fig. 2 Distribution of radial magnetic flux density along the thrust axis at the channel mean diameter. Magnetic field configuration could be adjusted by changing magnetic coil current

channel had an inner diameter of 14 mm and outer diameter of 26 mm. The main ion production and acceleration region was made of boron nitride. A magnetic coil placed at the center of the thruster head created a radial magnetic field near the channel exit. Figure 2 shows the distribution of radial magnetic flux density B_r along the channel center line, which was obtained by a direct measurement using a Gauss meter. In this work, we refer to the maximum radial magnetic flux density for each magnetic field condition as $B_{r,\max}$ and use it as the representative value. At the bottom of the discharge channel, an anode electrode was attached to apply anode voltage V_a, and the propellants were fed through it. The base of the thruster head was mounted on an aluminum panel whose temperature was well controlled by cooling water to prevent an excessive increase in the temperature of all components.

For thruster operations, we used a tungsten-filament plasma bridge cathode (LFN2000, Kaufman & Robinson) worked with xenon regardless of the anode propellant type. In all cases, the keeper voltage applied to the cathode body was set to approximately 25 V. The

cathode was mounted vertically to the thrust direction as shown in Fig. 1 (a). The electrical configuration of the integrated system is also displayed in Fig. 1 (a). The cathode common was grounded and all voltages were applied based on the ground potential in this study. The main driving current, called the discharge current I_d, was measured using a noncontact current probe (A622, Tectronix). In Fig. 1 (b), we show a picture of the actual thruster plume when using water vapor as a propellant.

Vacuum facility

The thruster operations were conducted in a vacuum chamber with a diameter of 1 m and length of 2.6 m. The chamber was evacuated using both a turbomolecular pump with 820 L/s of N_2 pumping speed and a cryopump of 2400 L/s. A cold cathode ionization gauge (PKR 251, Pfeiffer Vacuum) was attached to the chamber wall, and we confirmed that the base pressure was less than 10^{-3} Pa before each testing.

Gas feeding system

Water-vapor feeding system

A dedicated feeding system was constructed to supply a constant amount of water vapor. In this system, the anode mass flow rate $\dot{m}_a$ was controlled by the pressure in the accumulator p_{ac} connected upstream of the thruster head. According to a general mathematical analysis for viscous flow [34], the mass flow rate can be expressed as

$$\dot{m}_a = \frac{\pi r^4}{8\mu L}\frac{p_{ac}+p_b}{2}\frac{p_{ac}-p_b}{RT_g} \approx \frac{\pi r^4}{16\mu L}\frac{p_{ac}^2}{RT_g}, \tag{1}$$

where r is the effective radius and L is the effective length of the flow path, μ is the viscosity coefficient, R is the gas constant, T_g is the gas temperature, and p_b is the background pressure. In this formula, we assume that the flow path is approximated by a simple round tube and that the background pressure is considerably less than the accumulator pressure ($p_{ac} \gg p_b$). If the line shape and gas temperature at the choking point do not change significantly, Eq. (1) can be written as a function dominated by the accumulator pressure as follows:

$$\dot{m}_a \approx K p_{ac}^2, \tag{2}$$

where K is a coefficient that should be constant for each experiment.

The mechanical structure of the water-vapor feeding system is shown in Fig. 3. A regulator valve mounted between the water tank and accumulator was repeatedly opened and closed to maintain constant accumulator pressure. The cycle period was 200 ms and the duty ratio was controlled using a proportional-integral-derivative controller. To eliminate the temperature effect of the anode, a sufficiently small orifice was inserted at the accumulator exit to choke the flow. Heaters were attached to the system body and heated water to maintain the vapor pressure in the tank sufficiently greater than the accumulator pressure, which was managed between 40 and 50 °C. The system was used in a vacuum chamber to prevent unexpected condensation in the feeding line.

All operations using water vapor were performed with a constant accumulator pressure (= 5.0 kPa), and the actual mass flow rate was determined as the mass reduction rate of the

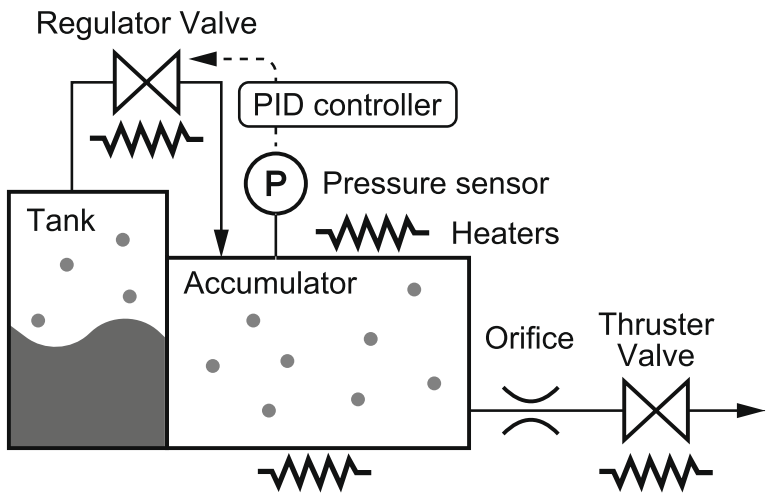

Fig. 3 Structural schematic of the water-vapor feeding system

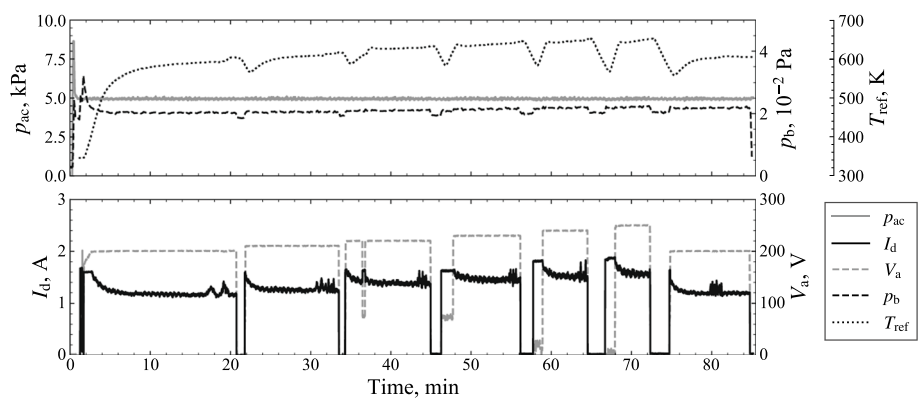

Fig. 4 Example of time history of operating parameters during experiment using water vapor

water tank. Before and after the experiment, we weighed the tank in the atmosphere using a mass balance and computed the mass difference Δm. For each vacuuming, water vapor of five times the accumulator volume was exhausted before firing to remove any internal air gas; thus, the mass difference would include the vapor mass released through this process. We estimated this using the gas equation and calculated the effective mass reduction by subtracting it from the mass difference. The anode mass flow rate was then obtained by dividing the effective mass reduction by the total feeding time t_{tot} as

$$\dot{m}_a = \frac{\Delta m - 5(\overline{p_{vap}} V_{ac} / R\overline{T_{vap}})}{t_{tot}}, \tag{3}$$

where $\overline{p_{vap}}$ is the average vapor pressure and $\overline{T_{vap}}$ is the average vapor temperature during the first exhaustion process, and V_{ac} is the accumulator volume. Figure 4 shows the typical time history of the accumulator pressure with other operating parameters. Throughout the experiment, the accumulator pressure was well controlled to be the target value, and the background pressure was virtually constant (2×10^{-2} Pa for N_2 correction). This indicates that the above method is valid for the mass flow rate evaluation.

The thruster was operated with water vapor five times on separate days, and mass flow rate determinations were performed in four of them. The measurement results are summarized in Table 1. The average mass flow rate was 0.81 mg/s with the uncertainty of ±7 % derived from Eq. (3) and the measurement variations.

Xenon feeding system

The xenon mass flow rate was controlled by mass flow controllers (S48-32, HORIBA) for both the anode and cathode. In every test with xenon propellant, the anode mass flow rate was set to 0.78 mg/s with an uncertainty of ±2 %, which was selected as a value close to the water-vapor mass flow rate determined in Section 2.3. The background pressure was 4×10^{-2} Pa for the N_2 correction when the thruster was running. As mentioned in Section 2.1, the cathode working gas was always xenon regardless of the anode propellant type, and the cathode mass flow rate was fixed to 0.06 mg/s in all anode conditions. This value was less than 10 % of the anode mass flow rate, and also less than 1 % of the water-vapor flow rate in the volumetric flow correction.

Instruments for plume diagnostics

Faraday probe

A nude Faraday probe with a copper collector and stainless-steel guard ring was used to measure the beam current profiles. The diameters of the collector and the guard ring outer edge were 10 mm and 20 mm, respectively, and the gap between them was 0.45 mm. During the measurements, both the collector and guard ring were biased to −20 V to repel electrons. The probe surface was swept in an arc with 19.8 cm of sweeping radius R_s by stepping motor. The collected ion current was measured using a shunt resistor and converted to ion flux density j_b as a function of the angular position. The total beam current $I_{b,tot}$ and axial beam current $I_{b,axis}$ were calculated as

$$I_{b,tot} = \pi R_s^2 \int_{-\pi/2}^{\pi/2} j_b(\theta) \sin(\theta) d\theta, \tag{4}$$

$$I_{b,axis} = \pi R_s^2 \int_{-\pi/2}^{\pi/2} j_b(\theta) \sin(\theta) \cos(\theta) d\theta, \tag{5}$$

where θ is the angle between the probe axis and thrust axis.

These integrated values could be overestimated by the effects of the collector materials or test facilities. Regarding the material effects, secondary electron emission (SEE) is one of the main concerns. Brown et al. recommended correcting the current density

Table 1 Summary of water-vapor flow rate measurements

No.	p_{ac}, kPa	V_a, V	t_{tot}, s	Δm, g	$\dot{m}_a$, mg/s
1	5.0	200	2581.8	2.192	0.814
2	5.0	200	2244.8	1.962	0.831
3	5.0	200 - 240	5215.4	4.254	0.798
4	5.0	200 - 250	5066.2	4.216	0.814

using the SEE yield γ_{SEE} [35]. However, there are no reliable data on the SEE yield by low-energy ion bombardment to a copper surface. We then used the general expression of $\gamma_{\mathrm{SEE}} \approx 0.016(\varepsilon_{\mathrm{iz}} - 2\varepsilon_{\phi})$ for the SEE corrections [36], where $\varepsilon_{\mathrm{iz}}$ is the ionization potential of a colliding ion and ε_{ϕ} is the work function of copper (= 4.46 eV [37]). As ionization potentials, we referred to the first ionization potential of a water molecule and xenon atom, which were 12.62 and 12.13 eV, respectively [38, 39]. Facility effects could also have a significant influence on the current density because of the relatively high background pressure in our laboratory system. It is known that high background pressure expands the beam divergence due to charge exchange collisions (CEX) and increases the total beam current due to neutral ingestions and Bohm ion flux from the background plasma [35]. In particular, the Bohm ion flux influences only the probe output, which can yield results inconsistent with the state of the discharge. To avoid excessive overestimation by this effect, we subtracted the average current density at ±90 degrees from the current density profile and used the subtracted values $(j_{\mathrm{b}}(\theta) - \bar{j}_{\mathrm{b}}(\pm\pi/2))$ to calculate Eqs. (4) and (5). According to the error analysis including the above factors by Brown et al. [35, 40], measurements by a Faraday probe have the inherent uncertainty of ±6 % for the total beam current, ±10 % for the axial beam current, and ±10 % for the ratio of them, respectively. The probe was swept three times for each condition, and the variations were sufficiently smaller than the inherent uncertainties.

Retarding potential analyzer

A retarding potential analyzer (RPA) with three grids was used to measure the beam ion voltage. The first grid was floated and the second grid was biased to −30 V to repel the primary electrons. The third grid, called the retarding grid, was used to repel ions with a voltage less than the retarding potential applied to this grid. The ions passing through the third grid were collected by a molybdenum collector connected to the ground via a shunt resistor. The RPA was placed 50 cm from the channel exit along the thrust axis. For each anode voltage, the retarding potential was swept from the ground potential to at least 300 V. By differentiating the measured current with the retarding potential, we obtained the ion voltage distribution function (IVDF) $f(V)$:

$$f(V) \propto -\frac{dI}{dV}. \tag{6}$$

The retarding voltage was swept three times, and for each collected current profile, the moving average was taken over a range of ±5 V before differentiation. The average ion voltage V_{ave} was then computed from the IVDF as

$$V_{\mathrm{ave}} = \frac{\int Vf(V)dV}{\int f(V)dV}, \tag{7}$$

where the integration interval was limited to ±50 V of the peak to avoid noise effects. Based on the comparison with an electrostatic analyzer done by Beal et al. [41], an RPA involves an uncertainty about half of the spectral half width [9]; thus, the uncertainty of the average ion voltage was considered ±6–9 %.

Performance analysis method

The thrust performance was estimated based on the results of the plume diagnostics. The thrust force T generated by electrostatic acceleration is expressed as [42]

$$T = \alpha F_{\mathrm{t}} I_{\mathrm{b,tot}} \sqrt{\frac{2M\overline{V_{\mathrm{b}}}}{e}} \tag{8}$$

$$= \alpha I_{\mathrm{b,axis}} \sqrt{\frac{2M(V_{\mathrm{ave}} - V_{\mathrm{p}})}{e}}, \tag{9}$$

where α is a correction factor for dissociative or multiply charged ions, F_{t} is the cosine of the effective thrust-vector angle ($= I_{\mathrm{b,axis}}/I_{\mathrm{b,tot}}$), M is the mass of the propellant molecule, $\overline{V_{\mathrm{b}}}$ is the beam acceleration voltage, and V_{p} is the beam plasma potential. The correction factor α and beam plasma potential are not determined from the measurements in this study. In terms of α, we approximated that all neutrals were ionized to singly charged original molecules ($\alpha \approx 1$) by the following reactions:

$$\mathrm{H_2O} + \mathrm{e}^- \rightarrow \mathrm{H_2O}^+ + 2\mathrm{e}^-, \tag{10}$$

$$\mathrm{Xe} + \mathrm{e}^- \rightarrow \mathrm{Xe}^+ + 2\mathrm{e}^-. \tag{11}$$

For xenon, the current fraction of Xe^+, Xe^{2+}, and Xe^{3+} in the Hall thruster plasma plume have been measured to be comparable in some previous studies [9, 15, 43], and the thrust error caused by the above approximation is estimated to be within 5 %. In the case of water vapor, on the other hand, the actual ion species and their abundance ratios in the plume have not been known. Instead, in reference to the previous research for a microwave discharge ion source [44], it was reported that OH^+, H_3O^+, and O^+ were mainly observed other than H_2O^+, and their existence were 15 %, 12 %, and 5 % of H_2O^+, respectively. The referenced results, however, are assumed to be derived from different plasma parameters from those of the Hall thruster discharge plasma. The typical electron temperature and density are 10–20 eV and 10^{17} m^{-3} for the microwave discharge ion source [45, 46], whereas 20–30 eV and 10^{18} m^{-3} for xenon Hall thrusters [47]. Although high temperature electrons additionally produce H^+ and H_2^+, the reaction rates for them are less than 1/10 of that producing H_2O^+ in the typical electron temperature regime [38]. Considering those investigations, it is reasonable to estimate the thrust error by $\alpha \approx 1$ of less than 10 % for water vapor. Regarding the beam plasma potential, we referred $V_{\mathrm{p}} = 25.7$ V that we measured using a planar Langmuir probe under a condition of $V_{\mathrm{a}} = 200$ V, $\dot{m}_{\mathrm{a}} = 0.59$ mg/s with xenon. We also used the same value for the analysis of water vapor based on the assumption that the beam plasma potential would be rather related to the cathode condition (e.g., cathode flow rate or keeper voltage), which was similar for water vapor and xenon. However, the actual plasma potential was indeed unclear; thus, we assumed the uncertainty to be ±50 % based on the variation in some previous reports [48–50].

In addition to the thrust force, we evaluated the anode specific impulse I_{spa} and anode efficiency η_{a} based on the following definitions using the obtained thrust values.

$$I_{\mathrm{spa}} \equiv \frac{T}{g\dot{m}_{\mathrm{a}}}, \tag{12}$$

$$\eta_a \equiv \frac{T^2}{2\dot{m}_{\mathrm{a}}P_{\mathrm{a}}}, \tag{13}$$

where g is the gravitational acceleration and P_{a} is the anode power defined as $I_{\mathrm{d}}V_{\mathrm{a}}$. The plume characteristics are also useful for efficiency analysis, which provides additional information regarding the thruster loss mechanism. Under the above approximations, the anode efficiency can be separated into a product of four internal efficiencies: mass utilization η_{m}, current utilization η_{c}, voltage utilization η_{v} and beam η_{b} efficiencies, as

$$\eta_a = \frac{1}{2\dot{m}_{\mathrm{a}}P_{\mathrm{a}}}\left(\alpha I_{\mathrm{b,axis}}\sqrt{\frac{2M(V_{\mathrm{ave}}-V_{\mathrm{p}})}{e}}\right)^2 \tag{14}$$

$$= \alpha^2 \cdot \underbrace{\frac{MI_{\mathrm{b,tot}}}{e\dot{m}_{\mathrm{a}}}}_{\eta_{\mathrm{m}}} \cdot \underbrace{\frac{I_{\mathrm{b,tot}}}{I_{\mathrm{d}}}}_{\eta_{\mathrm{c}}} \cdot \underbrace{\frac{V_{\mathrm{ave}}-V_{\mathrm{p}}}{V_{\mathrm{a}}}}_{\eta_{\mathrm{v}}} \cdot \underbrace{\left(\frac{I_{\mathrm{b,axis}}}{I_{\mathrm{b,tot}}}\right)^2}_{\eta_{\mathrm{b}}}, \tag{15}$$

where the mass utilization efficiency does not include the information of ion species in this expression. A detailed explanation of each term can be found in [40].

A performance analysis was conducted for anode voltage ranging from 200 to 240 V with both propellants. The magnetic field condition was determined based on the knowledge that the discharge current would be minimized under the optimal intensity [51]. The thrust performance can also be influenced by the thermal conditions [52], especially when using water vapor with a lighter molecular mass. Therefore, we monitored the anode-bottom temperature as a reference temperature T_{ref} using a thermocouple and began data acquisition after the temperature approached saturation. In Fig. 4, we also show the temperature transition during the experiment; it can be confirmed that the discharge current was virtually constant with the temperature saturation. Faraday probe and RPA measurements were conducted on different days, and the discharge current repeatability was ensured, as indicated in the following section.

Results and discussion

Discharge characteristics

Figure 5 (a) shows the dependency of the average discharge current on the magnetic flux density at 200 V. The discharge current was measured for at least three times on different days and the repeatability within ±4 % was confirmed. For both water vapor and xenon, the discharge current exhibited a minimum value at a certain magnetic field. In the case of water vapor, it was minimized under a lower magnetic flux density, and maintaining the discharge was difficult in the strong magnetic intensity region. The magnetic field conditions that minimize the discharge current were similar in the 200–240 V range for each propellant.

Figure 5 (b) shows the discharge current dependency on the anode voltage under the same magnetic field condition as the colored plot in Fig. 5 (a). The discharge current

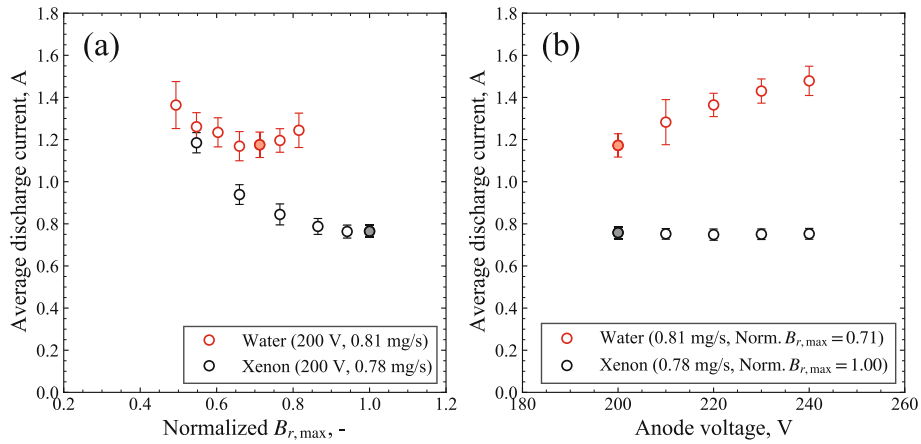

Fig. 5 Average discharge current as a function of (**a**) magnetic flux density $B_{r,\max}$ and (**b**) anode voltage V_a. The colored plots represent the same operation point respectively

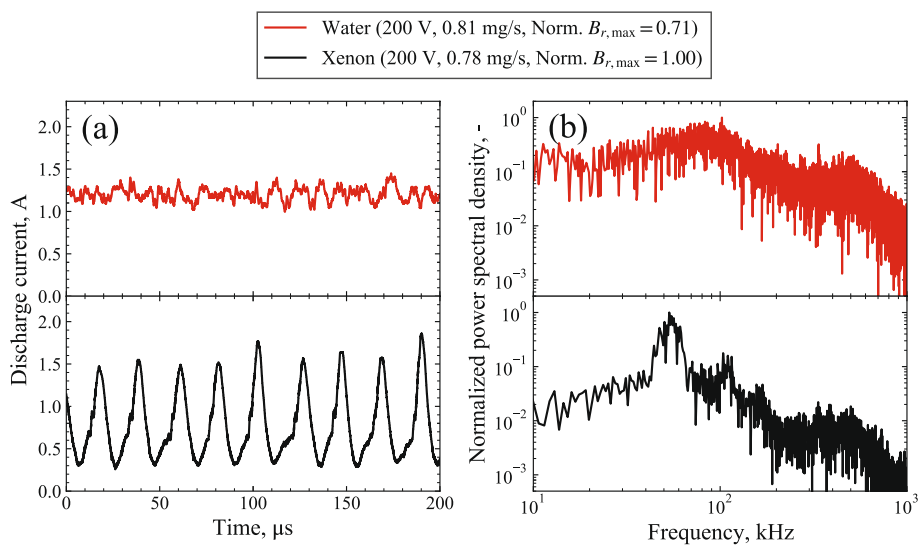

Fig. 6 (**a**) Typical waveform and (**b**) its power spectral density of discharge current oscillation with water vapor and xenon

increased with the anode voltage for water vapor, whereas there was virtually no correlation between them for xenon. By converting the anode flow rate to the current-equivalent flow rate, which was the value when all the propellant flux was assumed to become the singly charged ion current, the xenon flow rate was calculated to be 0.57 A, which was less than the discharge current. On the other hand, the water-vapor flow rate was 4.4 A in the current-equivalent conversion, which was more than 2.5 times greater than the discharge current. This suggests that water vapor was less ionized, whereas xenon was virtually fully ionized at 200 V. In general, increasing the anode voltage also increases the electron temperature in the discharge channel [47]; thus, ionization would be promoted at higher voltages in the case of water vapor.

Figure 6 shows the typical wave form and its power spectral density of the discharge current oscillation, which was obtained at the operating point shown as the colored

plot in Fig. 5. Focusing on the low-frequency band, the oscillation characteristics were different between the two propellants; xenon exhibited a large oscillation of nearly 50 kHz, called the "breathing mode", and a relatively small oscillation of nearly 100 kHz, whereas water vapor exhibited only a small oscillation around 100 kHz. The mechanism of the "breathing mode" is frequently explained as an instability resulting from the depletion of neutral particles due to ionization [42, 53]. From this point of view, it makes sense that the "breathing mode" amplitude of water vapor was smaller than that of xenon because the large existence of non-ionized neutrals was predicted.

Plume characteristics

The beam current and IVDFs were measured under discharge conditions corresponding to the plots in Fig. 5 (b). Figure 7 (a) shows the angular distributions of the beam current density at 200 and 240 V obtained by the Faraday probe. Comparing the two propellants, the xenon plumes were well focused within ±30 degrees, whereas the water-vapor plumes exhibited greater divergence with dented peaks. Figure 7 (b) shows the IVDFs, which are the negative first differentials of the RPA outputs, at the same anode voltages. The peak of the IVDF was shifted marginally to the lower side in the case of water vapor. In addition, ions with lower energies are relatively more distributed in the water-vapor plume.

The expansion of the beam divergence and the large existence of low-energy ions would be closely related because ions generated with low potential have less directionality. Two possible processes can be considered for the production of a low-energy ion: transition of a fast ion to a slow ion through collisions or ionization downstream of the main acceleration region. Of the former collisional effects, CEX is, in general, the most dominant. The influence of CEX can be deduced from the collision mean free path below.

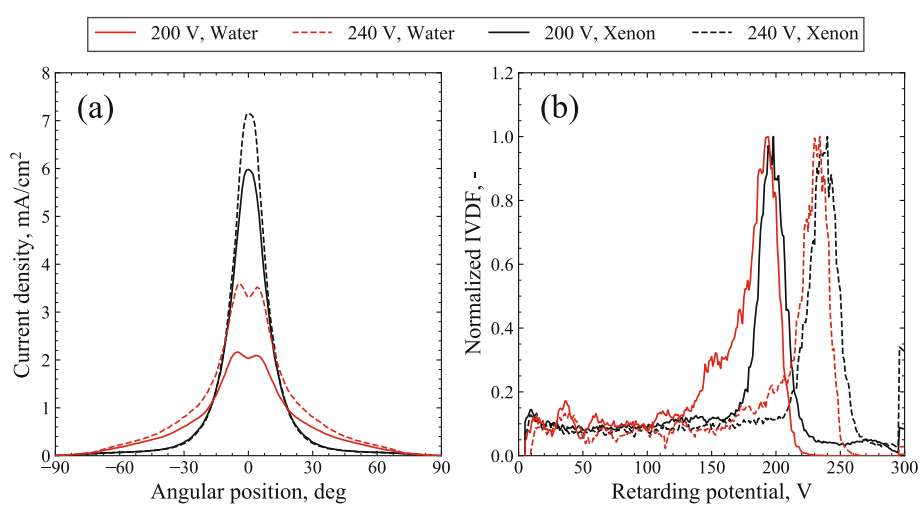

Fig. 7 (**a**) Beam current density distributions and (**b**) IVDFs of ion beams for water vapor and xenon at anode voltage of 200 and 240 V

$$\lambda_{\mathrm{CEX}} \equiv \frac{1}{\sigma_{\mathrm{CEX}} n_{\mathrm{n}}}, \tag{16}$$

where σ_{CEX} is the collision cross-section of the CEX and n_{n} is the neutral number density. For the effect of downstream ion production, an ionization mean free path should be an indication. If it significantly exceeds the channel length, ionization could progress beyond the acceleration region. The ionization mean free path is defined as

$$\lambda_{\mathrm{iz}} \equiv \frac{v_{\mathrm{n}}}{\langle \sigma_{\mathrm{iz}} v_{\mathrm{e}} \rangle n_{\mathrm{e}}}, \tag{17}$$

where v_{n} is the neutral velocity, $\langle \sigma_{\mathrm{iz}} v_{\mathrm{e}} \rangle$ is the ionization-reaction rate constant, and n_{e} is the electron number density. Here, we roughly calculate these mean free paths. The neutral number density is estimated from the mass flow rate as

$$n_{\mathrm{n}} \approx \frac{\dot{m}_{\mathrm{a}}}{M v_{\mathrm{n}} A}, \tag{18}$$

where A is the cross-sectional area of the discharge channel. Because this formula does not account for ionization, it provides the maximum possible value. The electron number density is estimated from the total beam current under the assumption of quasi-neutrality as

$$n_{\mathrm{e}} \simeq n_{\mathrm{i}} \approx \frac{I_{\mathrm{b,tot}}}{e v_{\mathrm{i}} A}, \tag{19}$$

where n_{i} is the ion number density and v_{i} is the ion velocity. In this analysis, we used the average axial thermal velocity ($= \sqrt{kT_{\mathrm{n}}/2\pi M}$, where T_{n} is the neutral temperature) and accelerated velocity ($= \sqrt{2e\overline{V_{\mathrm{b}}}/M}$) for the neutral and ion velocity, respectively. We only considered the reaction between a singly charged ion and neutral molecule in CEX, and used $\sigma_{\mathrm{CEX}} = 4.2 \times 10^{-20}\ \mathrm{m}^2$ for water vapor [54] and $\sigma_{\mathrm{CEX}} = 5.6 \times 10^{-19}\ \mathrm{m}^2$ for xenon [55]. Regarding the ionization reaction, we only addressed Reactions (10) and (11). These ionization reaction rates were computed as functions of electron temperature using the cross-section data in [38, 39]. From the set of equations above, the CEX and ionization mean free path were calculated using the experimental values ($\dot{m}_{\mathrm{a}}$, $I_{\mathrm{b,tot}}$, and V_{ave} at 200 V), with the assumption of $T_{\mathrm{n}} \approx 600$ K and $T_{\mathrm{e}} \approx 20$ eV. In Fig. 8, we show the results of this analysis and compare them with the ceramic channel-wall length L_{c}. To suppress low-energy ions, the CEX and ionization mean free path should satisfy the relationships of $\lambda_{\mathrm{CEX}} \gg L_{\mathrm{c}}$ and $\lambda_{\mathrm{iz}} \ll L_{\mathrm{c}}$. The CEX mean free paths of both propellants were sufficiently longer than the channel length, although they would be underestimated because of the neglect of ionized particles. Conversely, the ionization mean free path did not satisfy the above relationship only in the case of water. Therefore, it is suggested that the long ionization mean free path, rather than the CEX, contributes to the low-energy ion production. Other factors that expand the beam divergence are, for example, the magnetization of the accelerated ions or non-optimization of the magnetic field. Whether ions are magnetized or not can be determined from the ion Larmor radius r_{ic} ($= M v_{\mathrm{i}}/eB$). We calculated this for each propellant; the values are also shown in Fig. 8. As a result, the ion Larmor radius of H_2O^+ are greater than the channel length; thus, ion

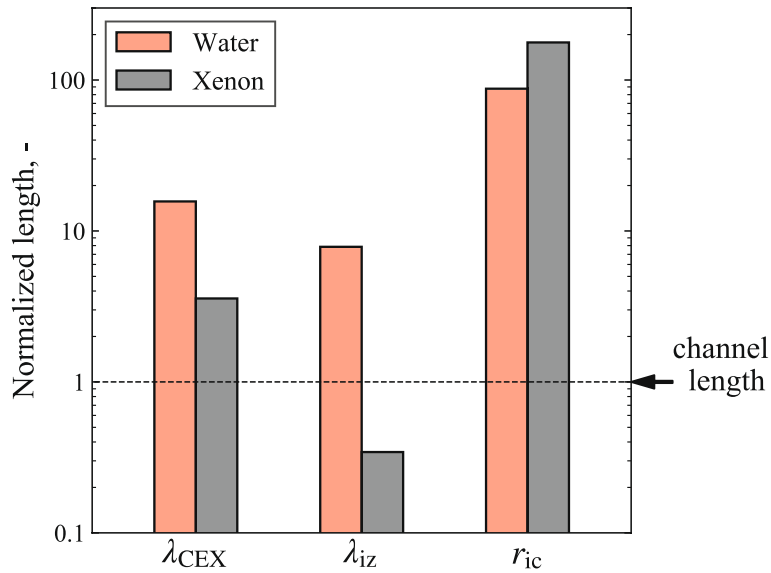

Fig. 8 CEX mean free paths, ionization mean free paths and ion Larmor radiuses of H_2O^+ and Xe^+. Those values were calculated with the assumption of $T_n \approx 600$ K, $T_e \approx 20$ eV

Table 2 Operating parameters and estimated thrust performance

Propellant	$\dot{m}_a$, mg/s	V_a, V	I_d, A	P_a, W	T, mN	T/P_a, mN/kW	I_{spa}, s	η_a, %
Water	0.81 ± 0.06	200 ± 0.7	1.16 ± 0.06	233 ± 11	4.4 ± 0.7	19 ± 3	550 ± 100	5 ± 2
Water	0.81 ± 0.06	240 ± 0.7	1.49 ± 0.07	358 ± 17	6.8 ± 1.0	19 ± 3	860 ± 140	8 ± 3
Xenon	0.78 ± 0.02	200 ± 0.7	0.76 ± 0.03	153 ± 6	10.3 ± 1.3	67 ± 9	1340 ± 170	44 ± 12
Xenon	0.78 ± 0.02	240 ± 0.7	0.75 ± 0.03	180 ± 6	11.8 ± 1.4	66 ± 8	1540 ± 190	50 ± 13

magnetization would not be a critical issue. The effect of magnetic field optimization is more difficult to evaluate analytically because it involves the nonlinearity of the plasma wall sheath. We will investigate the dependency on the magnetic field in more detail in future experiments.

Performance estimation

Table 2 lists the estimated thrust performance with total uncertainties of water and xenon propellants at the minimum and maximum anode voltages. In addition, Fig. 9 shows the four efficiencies defined in Eq. (14) as a function of anode voltage. It should be noted that the indirect performance determination from plume diagnostics has low reliability, as suggested by the large uncertainties in Table 2; thus, the results should be validated by direct thrust measurements using a thrust balance in the future study. We also suppose that the computed values could be overestimated due to the relatively high background pressure. Previous studies have proved that an increase in background pressure results in artificial improvement of thruster performances because of neutral ingestion from the test facility [56]. Considering that the anode efficiencies of other 100 W-class Hall thrusters are distributed between 20 and 40 % [33], the anode efficiencies calculated in this study could be estimated 1.5–2 times higher than the actual. The

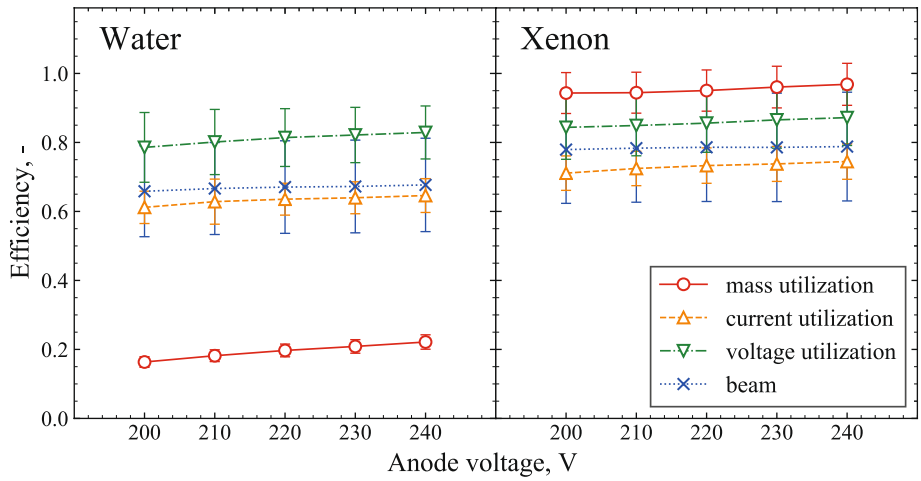

Fig. 9 Current utilization efficiency, voltage utilization efficiency, mass utilization efficiency, and beam efficiency of water vapor and xenon as a function of anode voltage

similar degrees of overestimation can also be included in the computed performance of water vapor. As well as the direct thrust validations, the evaluation and modification of the facility neutral effects is one of the future issues.

Focusing on the performance of water vapor, the thrust-to-power ratio and specific impulse were 19 mN/kW and 550–860 s at 200–240 V, respectively. In Fig. 9, the mass utilization efficiency indicates by far the lowest value among the efficiencies as suggested in the above sections, which causes deterioration of the specific impulse. Theoretically, if the mass utilization efficiency is improved to nearly 40 %, the specific impulse could be as high as that of xenon. From the neutral continuity equation, the ionization fraction ζ_{iz} is written as a function of the ionization mean free path [47]:

$$\zeta_{\mathrm{iz}} = 1 - \exp(-L_{\mathrm{iz}}/\lambda_{\mathrm{iz}}), \tag{20}$$

where L_{iz} is an effective ionization length. From Fig. 8, it is clear that the long ionization mean free path of water reduces the ionization fraction. A possible strategy for ionization improvement is to increase the discharge voltage, which can increase the electron temperature in the discharge plasma. In fact, the mass utilization efficiency improved by 6 % when the voltage was increased from 200 to 240 V in this experiment. Extending the ionization length is another solution for improving the ionization fraction. An extended channel [57, 58] can be used for this purpose. However, a long discharge channel also increases plasma-wall interactions that contribute to ion losses; thus, we must also consider the magnetic field design as it effectively confines the plasma.

Water-electron reactions not only consume energy for ionization or excitation, but also rotation, vibration, attachment, and dissociation as a nature of polyatomic molecules. For the power loss evaluation, we introduce the effective ionization cost [40] as

$$\varepsilon_{\mathrm{iz}} = \frac{P_{\mathrm{a}} - P_{\mathrm{jet}}}{I_{\mathrm{b,tot}}}, \tag{21}$$

where P_{jet} is the accelerated jet power defined as $I_{\mathrm{b,tot}}\overline{V_{\mathrm{b}}}$. From the results in Table 2, the effective ionization costs were calculated as 170 W/A for water vapor and 113 W/A for

xenon at 200 V. Because the ionization potentials are not significantly different between water (Reaction (10)) and xenon (Reaction (11)), the unique reactions of water vapor should contribute considerably to the additional energy cost. However, the effective ionization cost of water vapor exhibited a small variation in the anode voltage, which was ±2 % for 200–240 V. This indicates that the voltage increase in this range is more beneficial for improving the ionization fraction than the negative influence of the energy loss. According to Itikawa et al. [38], the reaction rates of dissociative reactions (dissociation and dissociative ionization) increase significantly with the ionization reaction rate above an electron temperature of 10 eV. Therefore, operating with excessive voltage could waste input power and produce low-momentum ions of H^+. However, the effects of the dissociative ions cannot be truly identified from this analysis because we assumed only H_2O^+. To gain more insight into the energy and momentum loss mechanisms, information regarding the ion species is required. High-voltage operation also leads to an increase in the total power consumption if the propellant feeding is constant. That is, reducing the mass flow rate is necessary for low-power applications, which is another issue for further development.

Conclusion

A Hall thruster using water vapor as a propellant was proposed for the primary propulsion of a small spacecraft and experimentally demonstrated in ground testing. Its discharge and plume characteristics were measured for anode voltages ranging from 200 to 240 V and compared with those of xenon. The average discharge current of each propellant exhibited similar downward convex dependency on the magnetic flux density. However, it had a different trend with respect to the anode voltage; it increased with a rise of the voltage for water vapor,whereas it was virtually constant for xenon. In higher time resolutions, the discharge current of the water vapor exhibited a relatively small oscillation, which seemed different from "breathing mode" that was observed when using xenon. In terms of plume characteristics, the water-vapor plasma plume was more divergent and contained more low-energy ions. All of these unique features of the water-vapor Hall thruster were deduced to be mainly due to insufficient ionization in the discharge channel.

As a result of the thrust performance analysis based on plume diagnostics, a thrust-to-power ratio of 19 mN/kW, specific impulse of 550–860 s, and anode efficiency of 5–8 % were estimated for the anode power ranging from 233 to 358 W, although these values could be positively influenced by 10^{-2} Pa order of the background pressure and should be validated by direct thrust measurements in the future. An efficiency analysis revealed that the mass utilization efficiency was the lowest among the internal efficiencies, as indicated by the discharge and plume characteristics. In addition, power utilization was also evaluated using an effective ionization cost, which suggested that the water propellant would consume additional power for reactions unique to polyatomic molecules. For the range investigated in this study, an increase in the anode voltage also increased the water mass utilization efficiency with virtually constant ionization costs; thus, operating at a higher voltage could be more suitable for the use of water vapor. This study was conducted using a thruster head designed for a xenon propellant, and its achievable performance and requirements were clarified using water vapor as a propellant. Based on the results of this study, the thruster design and operating parameters should be modified for water vapor to achieve more practical performance.

Acknowledgements
This work was supported by MEXT Coordination Funds for Promoting AeroSpace Utilization; Grant Number JPJ000959.

Code availability
Not applicable.

Authors' contributions
All authors contributed to the study conception and design. Thruster design and development were performed by Kento Shirasu with advice from Hiroyuki Koizumi, Hiroki Watanabe, Yuichi Nakagawa and Kimiya Komurasaki. The design and development of the water-vapor feeding system were performed by Yuichi Nakagawa and Kento Shirasu. Electrostatic probes for plume diagnostics were lent from Kimiya Komurasaki and Hiroki Watanabe. Facility preparations were performed by Kento Shirasu, Hiroki Kuwabara and Hokuto Sekine. Data collection and analysis were performed by Kento Shirasu and Masayuki Matsuura. The first draft of the manuscript was written by Kento Shirasu and all authors commented on the previous versions of the manuscript. All authors read and approved the final manuscript.

Funding
This work was supported by MEXT Coordination Funds for Promoting AeroSpace Utilization; Grant Number JPJ000959.

Availability of data and materials
The data that support the findings of this study are available from the corresponding author upon reasonable request.

Declarations

Competing interests
The authors declare no competing interests.

Received: 25 November 2022 Accepted: 15 March 2023
Published online: 27 March 2023

References

1. Freeman A (2020) Exploring our solar system with CubeSats and SmallSats: the dawn of a new era. CEAS Space J 12(4):491–502. https://doi.org/10.1007/s12567-020-00298-5
2. Curzi G, Modenini D, Tortora P (2020) Large constellations of small satellites: A survey of near future challenges and missions. Aerospace 7(9):133. https://doi.org/10.3390/aerospace7090133
3. Kuninaka H, Nishiyama K, Funaki I, Yamada T, Shimizu Y, Kawaguchi J (2007) Powered flight of electron cyclotron resonance ion engines on hayabusa explorer. J Propul Power 23(3):544–551. https://doi.org/10.2514/1.25434
4. Hosoda S, Nishiyama K, Tsukizaki R (2022) Chapter 20 - ion engine system of hayabusa2. In: Hirabayashi M, Tsuda Y (eds) Hayabusa2 Asteroid Sample Return Mission, pp 401–414. https://doi.org/10.1016/B978-0-323-99731-7.00020-9
5. Koizumi H, Kuninaka H (2010) Miniature microwave discharge ion thruster driven by 1 watt microwave power. J Propul Power 26(3):601–604. https://doi.org/10.2514/1.45194
6. Tsay M, Frongillo J, Zwahlen J, Paritsky L (2016) Maturation of iodine fueled BIT-3 RF ion thruster and RF neutralizer. In: 52nd AIAA/SAE/ASEE Joint Propulsion Conference, Salt Lake City, USA. https://doi.org/10.2514/6.2016-4544
7. Szabo JJ, Tedrake R, Metivier E, Paintal S, Taillefer Z (2017) Characterization of a one hundred watt, long lifetime hall effect thruster for small spacecraft. In: 53rd AIAA/SAE/ASEE Joint Propulsion Conference, Atlanta, USA. https://doi.org/10.2514/6.2017-4728
8. Mazouffre S, Grimaud L (2018) Characteristics and performances of a 100-W hall thruster for microspacecraft. IEEE Trans Plasma Sci IEEE Nucl Plasma Sci Soc 46(2):330–337. https://doi.org/10.1109/TPS.2017.2786402
9. Watanabe H, Cho S, Kubota K (2020) Performance and plume characteristics of an 85 W class hall thruster. Acta Astronaut 166:227–237. https://doi.org/10.1016/j.actaastro.2019.07.042
10. Koizumi H, Kawahara H, Yaginuma K, Asakawa J, Nakagawa Y, Nakamura Y, Kojima S, Matsuguma T, Funase R, Nakatsuka J, Komurasaki K (2016) Initial flight operations of the miniature propulsion system installed on small space probe: PROCYON. Trans Jpn Soc Aeronaut Space Sci 14(ists30):Pb_13–Pb_22. https://doi.org/10.2322/tastj.14.Pb_13
11. Lascombes P, Montès M, Fiorentino A, Gelu T, Fillastre M, Gurciullo A (2021) Lessons learnt from operating the first cubesat mission equipped with a hall thruster. In: 35th Annual Small Satellite Conference, Utah, USA. SSC21-XI-01
12. Koizumi H, Komurasaki K, Aoyama J, Yamaguchi K (2014) Engineering model of the miniature ion propulsion system for the nano-satellite: HODOYOSHI-4. Trans Jpn Soc Aeronaut Space Sci 12(ists29):Tb_19–Tb_24. https://doi.org/10.2322/tastj.12.Tb_19
13. Hopkins MA, King LB (2014) Magnesium hall thruster with active thermal mass flow control. J Propul Power 30(3):637–644. https://doi.org/10.2514/1.B34888
14. Tirila VG, Ryan C, Demairé A, Hallock A (2022) Performance investigation of zinc propellant in sub kw class hall thrusters. In: 37th International Electric Propulsion Conference, Massachusetts, USA. IEPC-2022-281
15. Szabo J, Pote B, Paintal S, Robin M, Hillier A, Branam RD, Huffmann RE (2012) Performance evaluation of an Iodine-Vapor hall thruster. J Propul Power 28(4):848–857. https://doi.org/10.2514/1.B34291
16. Bretti MA (2022) Progress and developments of ultra-compact 10 watt class adamantane fueled hall thrusters for picosatellites. In: 37th International Electric Propulsion Conference, Massachusetts, USA. IEPC-2022-349
17. Benavides GF, Kamhawi H, Mackey J, Haag T, Costa G, (2018) Iodine Hall-Effect electric propulsion system research, development, and system durability demonstration. In: 2018 Joint Propulsion Conference. Ohio, USA. https://doi.org/10.2514/6.2018-4422

18. Thompson SJ, VanGermert JJ, Farnell CC, Farnell CC, Farnell SC, Hensen TJ, Ham R, Williams DD, Chandler JP, Williams JD (2019) Development of an iodine compatible hollow cathode. In: AIAA Propulsion and Energy 2019 Forum, Indiana, USA. https://doi.org/10.2514/6.2019-3997
19. Polzin KA, Peeples SR, Seixal JF, Mauro SL, Lewis BL, Jerman GA, Calvert DH, Dankanich J, Kamhawi H, Hickman TA, Szabo J, Pote B, Lee L (2015) Propulsion system development for the iodine satellite (iSAT) demonstration mission. In: Joint Conference of 30th International Symposium on Space Technology and Science, 34th International Electric Propulsion Conference and 6th Nano-satellite Symposium, Kobe, Japan. IEPC-2015-09
20. Martinez J, Rafalskyi D, Aanesland A (2019) Development and testing of the NPT30-I2 iodine ion thruster. In: 36th International Electric Propulsion Conference, Vienna, Austria. IEPC-2019-811
21. Pallichadath V, Turmaine L, Melaika A, Gelmi S, Ramisa MV, Rijlaarsdam D, Silva MAC, Guerrieri DC, Uludag MS, Zandbergen B, Cervone A (2019) In-orbit micro-propulsion demonstrator for PICO-satellite applications. Acta Astronaut 165:414–423. https://doi.org/10.1016/j.actaastro.2019.09.004
22. Nishii K, Asakawa J, Kikuchi K, Akiyama M, Wang Q, Murohara M, Ataka Y, Koizumi H, Funase R, Komurasaki K (2020) Flight model development and ground demonstration of water resistojet propulsion system for CubeSats. Trans Jpn Soc Aeronaut Space Sci 63(4):141–150. https://doi.org/10.2322/tjsass.63.141
23. Porter A, Freedman M, Grist R, Wesson C, Hanson M (2021) Flight qualification of a water electrolysis propulsion system. In: 35th Annual Small Satellite Conference, Utah, USA. SSC21-XI-06
24. Sheppard AJ, Little JM (2022) Performance analysis of an electron cyclotron resonance thruster with various propellants. J Propul Power 38(6):998–1008. https://doi.org/10.2514/1.B38698
25. Nakagawa Y, Koizumi H, Kawahara H, Komurasaki K (2019) Performance characterization of a miniature microwave discharge ion thruster operated with water. Acta Astronaut 157:294–299. https://doi.org/10.1016/j.actaastro.2018.12.031
26. Ataka Y, Nakagawa Y, Koizumi H, Komurasaki K (2021) Improving the performance of a water ion thruster using biased electrodes. Acta Astronaut 187:133–140. https://doi.org/10.1016/j.actaastro.2021.06.020
27. Koizumi H, Asakawa J, Nakagawa Y, Nishii K, Takao Y, Nakano M, Funase R (2019) Assessment of micropropulsion system unifying water ion thrusters and water resistojet thrusters. J Spacecr Rockets 56(5):1400–1408. https://doi.org/10.2514/1.A34407
28. Nakagawa Y, Tomita D, Koizumi H, Komurasaki K (2018) Design and test of a 100 μN-class thrust stand for a miniature water ion thruster with CubeSat. Trans Jpn Soc Aeronaut Space Sci 16(7):673–678. https://doi.org/10.2322/tastj.16.673
29. Goebel DM, Watkins RM, Jameson KK (2007) LaB6 hollow cathodes for ion and hall thrusters. J Propul Power 23(3):552–558. https://doi.org/10.2514/1.25475
30. Schwertheim A, Knoll A (2022) Experimental investigation of a water electrolysis hall effect thruster. Acta Astronaut 193:607–618. https://doi.org/10.1016/j.actaastro.2021.11.002
31. Mazouffre S (2016) Electric propulsion for satellites and spacecraft: established technologies and novel approaches. Plasma Sources Sci Technol 25(3):033002. https://doi.org/10.1088/0963-0252/25/3/033002
32. Dannenmayer K, Mazouffre S (2011) Elementary scaling relations for hall effect thrusters. J Propul Power 27(1):236–245. https://doi.org/10.2514/1.48382
33. Hallouin T, Mazouffre S (2020) Far-Field plume characterization of a 100-W class hall thruster. Aerospace 7(5):58. https://doi.org/10.3390/aerospace7050058
34. Jorisch W (2014) Fundamentals of Vacuum Technology. In: Jorisch W (ed) Vacuum Technology in the Chemical Industry. Wiley-VHC Verlag & Co. KGaA, Weinheim, Germany, p 1–14
35. Brown DL, Walker MLR, Szabo J, Huang W, Foster JE (2017) Recommended practice for use of faraday probes in electric propulsion testing. J Propul Power 33(3):582–613. https://doi.org/10.2514/1.B35696
36. Lieberman MA, Lichtenberg AJ (2005) Principles of Plasma Discharges and Materials Processing, 2nd ed. John Wiley & Sons, Inc., Hoboken
37. Anderson PA (1949) The work function of copper. Phys Rev 76(3):388–390. https://doi.org/10.1103/PhysRev.76.388
38. Itikawa Y, Mason N (2005) Cross sections for electron collisions with water molecules. J Phys Chem Ref Data 34(1):1–22. https://doi.org/10.1063/1.1799251
39. Mathur D, Badrinathan C (1987) Ionization of xenon by electrons: Partial cross sections for single, double, and triple ionization. Phys Rev A Gen Phys 35(3):1033–1042. https://doi.org/10.1103/physreva.35.1033
40. Brown DL, Larson CW, Beal BE, Gallimore AD (2009) Methodology and historical perspective of a hall thruster efficiency analysis. J Propul Power 25(6):1163–1177. https://doi.org/10.2514/1.38092
41. Beal BE, Gallimore AD (2003) Energy analysis of a hall thruster cluster. In: 28th International Electric Propulsion Conference, Toulouse, France. IEPC-2003-035
42. Goebel DM, Katz I (2008) Fundamentals of Electric Propulsion: Ion and Hall Thrusters. John Wiley & Sons Inc, Hoboken
43. Reid B, Shastry R, Gallimore A, Hofer R (2008) Angularly-resolved exb probe spectra in the plume of a 6-kw hall thruster. In: 44th AIAA/ASME/SAE/ASEE Joint Propulsion Conference & Exhibit, Connecticut, USA. https://doi.org/10.2514/6.2008-5287
44. Nakagawa Y, Koizumi H, Naito Y, Komurasaki K (2020) Water and xenon ecr ion thruster–comparison in global model and experiment. Plasma Sources Sci Technol 29(10):105003. https://doi.org/10.1088/1361-6595/aba2ac
45. Sato Y, Koizumi H, Nakano M, Takao Y (2020) Electron loss mechanisms in a miniature microwave discharge water neutralizer. Phys Plasmas 27(6):063505. https://doi.org/10.1063/5.0002336
46. Sekine H, Minematsu R, Ataka Y, Ominetti P, Koizumi H, Komurasaki K (2022) Experimental characterization of non-maxwellian electron energy distributions in a miniaturized microwave plasma neutralizer. J Appl Phys 131(9):093302. https://doi.org/10.1063/5.0069600
47. Boeuf JP (2017) Tutorial: Physics and modeling of hall thrusters. J Appl Phys 121(1):011101. https://doi.org/10.1063/1.4972269

48. Frieman JD, Walker JA, Walker MLR, Khayms V, King DQ (2016) Electrical facility effects on hall thruster cathode coupling: Performance and plume properties. J Propul Power 32(1):251–264. https://doi.org/10.2514/1.B35683
49. Sommerville JD, King LB (2011) Hall-effect thruster-cathode coupling, part i: Efficiency improvements from an extended outer pole. J Propul Power 27(4):744–753. https://doi.org/10.2514/1.50123
50. Jorns BA, Byrne MP (2021) Model for the dependence of cathode voltage in a hall thruster on facility pressure. Plasma Sources Sci Technol 30(1):015012. https://doi.org/10.1088/1361-6595/abd3b6
51. Kim V (1998) Main physical features and processes determining the performance of stationary plasma thrusters. J Propul Power 14(5):736–743. https://doi.org/10.2514/2.5335
52. Book CF, Walker MLR (2010) Effect of anode temperature on hall thruster performance. J Propul Power 26(5):1036–1044. https://doi.org/10.2514/1.48028
53. Boeuf JP, Garrigues L (1998) Low frequency oscillations in a stationary plasma thruster. J Appl Phys 84(7):3541–3554. https://doi.org/10.1063/1.368529
54. Lishawa CR, Dressler RA, Gardner JA, Salter RH, Murad E (1990) Cross sections and product kinetic energy analysis of H2O+-H2O collisions at suprathermal energies. J Chem Phys 93(5):3196–3206. https://doi.org/10.1063/1.458852
55. Miller JS, Pullins SH, Levandier DJ, Chiu YH, Dressler RA (2002) Xenon charge exchange cross sections for electrostatic thruster models. J Appl Phys 91(3):984–991. https://doi.org/10.1063/1.1426246
56. Frieman JD, Liu TM, Walker MLR (2017) Background flow model of hall thruster neutral ingestion. J Propul Power 33(5):1087–1101. https://doi.org/10.2514/1.B36269
57. Yamasaki J, Yokota S, Shimamura K (2019) Performance enhancement of an argon-based propellant in a hall thruster. Vacuum 167:520–523. https://doi.org/10.1016/j.vacuum.2018.09.042
58. Marchioni F, Cappelli MA (2021) Extended channel hall thruster for air-breathing electric propulsion. J Appl Phys 130(5):053306. https://doi.org/10.1063/5.0048283

Publisher's Note

Springer Nature remains neutral with regard to jurisdictional claims in published maps and institutional affiliations.